

Calculating the Bohr Magneton using electron transitions in Mercury due to the Zeeman Effect

Darin Momayezi

Georgia Institute of Technology, Department of Physics

(Dated: October 15, 2023)

Abstract: In this study, we use the Zeeman Effect to measure the value of the Bohr magneton by studying atomic transitions in Mercury. Mercury lamps are easily sourced and have only two optically active electrons, which makes it well-suited for experimental study. An interference pattern is used to experimentally measure the atomic transitions that are combined with theory to calculate the value of the Bohr magneton.

Keywords: Zeeman Effect, Mercury, Bohr Magneton, Atomic Spectrum, Addition of Angular Momentum, Spin-Orbit Coupling, Fabry-Pérot Interferometer

I. INTRODUCTION

The Zeeman effect was discovered in 1896 by Peter Zeeman who observed the splitting of spectral lines in the presence of a static magnetic field. Zeeman suspected that oscillations of an electron in an atom could produce light and, therefore, would be affected by a magnetic field. His predictions were later corrected by quantum theory, which quantizes light, but Zeeman's observations illuminate rich atomic structure and won a Nobel prize in 1902. The appearance of spectral line splittings shows an underlying structure of the atom governed by selection rules based in quantum mechanics. Zeeman was right in predicting that the presence of a static magnetic field would affect the electron's behavior in the atom, but it is due to the interaction of its spin and angular quantum degrees of freedom with an externally applied magnetic field.

Quantum theory says that the electron possesses an intrinsic spin, which produces a magnetic dipole and is associated with a magnetic moment μ_s . The electron also orbits the nucleus with some angular momentum \mathbf{l} , which produces another magnetic dipole due to the movement of a charged particle. The elemental measure of magnetic moment is the Bohr magneton, μ_b , in the same way that the Coulomb, e , is the fundamental unit of electric charge. In this study, we use the Zeeman effect, which produces line splittings in the green spectrum of Mercury due to the interaction between a static magnetic field and the combined magnetic dipole of valence electrons of Mercury, to calculate the Bohr magneton.

The discovery of the Zeeman effect is a critical point in the history of Quantum Mechanics and Atomic Physics, and it is, therefore, essential to understand the structure of atoms. Although current literature simply uses the name "Zeeman effect", as we do here, it is historically separated into the "normal" and "anomalous" Zeeman effects since they were discovered separately. "Anomalous" refers to the fact that neither the electron spin nor the quantization of angular momentum had yet been discovered, so there was no good explanation for the anomalous Zeeman effect, while the normal Zeeman effect was predicted by electromagnetic theory. The anomalous Zeeman effect is produced by selection rules that are funda-

mentally quantum in nature. As mentioned before, the electron is associated with magnetic dipole moments due to its spin and angular momenta, which can be considered independently or must be coupled via the spin-orbit interaction (SOI) depending on the energy scale of interest. The study of atomic structure is the study of interactions and energy scales. There is a hierarchy of energy scales within the atom including the gross, fine and hyperfine structures. Beyond the general atomic structure given by the familiar principle (n), angular (l), and magnetic (m) quantum numbers, there are several relativistic corrections that are responsible for the fine (lower energy) structure where these numbers are no longer good quantum numbers. The theory of addition of angular momentum becomes essential to forming a basis for studying the atomic structure at the lower energy scales.

In the case of the Zeeman effect, the strength of the externally applied magnetic field determines which structures are most affected and, therefore, which interactions must be taken into account. As the electron orbits the nucleus it produces a magnetic field, or from the electron's point of view, the nucleus orbiting the electron produces a magnetic field of about $1-4$ gauss. The electron interacts with the magnetic field produced by its orbital motion, which couples with the electron's spin magnetic moment through the spin-orbit interaction. The magnetic field seen by the electron is much larger than the fields produced in the lab, therefore, the spin-orbit coupling is not negligible and the applied magnetic field is treated as a perturbation to the spin-orbit Hamiltonian

$$E_{ZE} \ll E_{s-o}. \quad (1)$$

Knowledge of the spin-orbit interaction is necessary to understand the atomic transitions that produce spectral line splittings in the presence of an external magnetic field. Since the energy produced by atomic transitions due to the Zeeman effect is proportional to the Bohr magneton μ_b (see §II. Theory), the fundamental unit of magnetic moment, μ_b can be calculated using experimental observations of the Zeeman effect.

Having introduced the importance of and motivation for observing the Zeeman effect, section II provides the

theoretical prediction of the Zeeman effect due to quantum theory

II. THEORY

A. Classical Bohr Magneton [1]

The electron orbiting the nucleus at the Bohr radius, the distance of the first Bohr orbit from the nucleus, can be modeled classically as a current carrying loop with current I and area $A = \pi r_B^2$, where r_B is Bohr radius. The current I is the amount of charge that passes through the loop per orbital period T ,

$$I = \frac{e}{T} = \frac{e}{\left(\frac{2\pi r_B}{v}\right)} = \frac{ev}{2\pi r_B} = \frac{e\hbar}{2\pi m r_B^2}, \quad (2)$$

where $v = \frac{\hbar}{r_B m}$ is the velocity of the orbiting electron and m is its mass. According to electromagnetic theory, a current carrying loop also possesses a magnetic moment, since it experiences a torque due to the Lorentz force in the presence of an external magnetic field \mathbf{B} ,

$$\mu_B = |I \cdot \vec{A}| = \frac{e\hbar}{2\pi m r_B^2} \pi r_B^2 = \frac{e\hbar}{2m} \approx 9.274 \cdot 10^{-24} \text{ J/T}. \quad (3)$$

While treating the electron as a classical current carrying loop is not the correct physical picture as described by quantum mechanics, it is sometimes good enough and predicts the correct value for the Bohr magneton μ_B . To experimentally measure μ_B with the Zeeman effect, however, we need to embark on a fully quantum mechanical treatment of the atom. In the next section, we give a quantum mechanical treatment of the atom to explain the properties of light emitted by mercury in an external magnetic field due to certain atomic transitions.

B. Addition of Angular Momenta

In atoms, such as Mercury, that have two optically active electrons, the electrostatic repulsion of the electrons, called the residual electrostatic energy E_{re} , causes their orbital angular momentum \mathbf{l} to change direction, however, their magnitudes do not [2]. Therefore, the total angular momentum $\mathbf{L} = \mathbf{l}_1 + \mathbf{l}_2$ is a good quantum number, which means \mathbf{L} is fixed and so its z-projection M_L . We may also combine the spins of the electrons into a total spin number $\mathbf{S} = \mathbf{s}_1 + \mathbf{s}_2$ to ensure a totally antisymmetric wavefunction as required by the Pauli-exclusion principle. \mathbf{L} and \mathbf{S} are good quantum numbers that take on the values $|\mathbf{l}_1 - \mathbf{l}_2| \leq \mathbf{L} \leq \mathbf{l}_1 + \mathbf{l}_2$ and $|\mathbf{s}_1 - \mathbf{s}_2| \leq \mathbf{S} \leq \mathbf{s}_1 + \mathbf{s}_2$, respectively. They form a new basis of states given by $|LM_LSM_S\rangle$ and term levels denoted as ^{2S+1}L ; this is known as the Russel-Saunders or LS-coupling scheme. In atoms with two optically active electrons, fine structure

arises from the interaction of the spin and angular momentum degrees of freedom called the spin-orbit interaction, given by the energy E_{s-o} . The fine structure of Mercury is best modeled by the spin-orbit interaction acting as a perturbation on the LS-coupled states $|LM_LSM_S\rangle$, i.e. $E_{s-o} \ll E_{re}$ [2]. In this case, the spin-orbit interaction causes total orbital angular momentum and the total spin angular momentum to interact so that they change direction, however, the total angular momentum $\mathbf{J} = \mathbf{L} + \mathbf{S}$ and its projection J_z are fixed in the absence of any external torque. Since \mathbf{L} and \mathbf{S} are still good quantum numbers, but their projections M_L and M_S are not, the new basis becomes $|JLSM_J\rangle$. This basis gives new term levels denoted by $^{2S+1}L_J$, which are shifted from the old term levels by the spin-orbit energy E_{s-o} . The angular momentum addition schemes discussed are motivated by the vector model below provided by Foot, which depicts the addition scheme pertaining to the fine structure of Mercury.

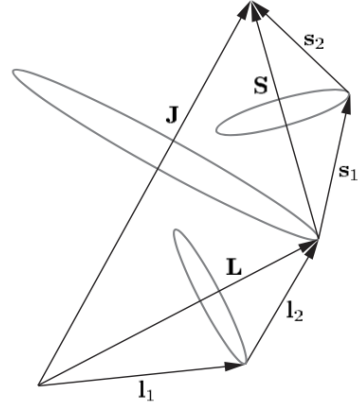


FIG. 1. LS-Coupling Fine Structure Vector Model [2]

In summary, the fine structure of Mercury is described in the basis $|JLSM_J\rangle$, where L and S are the total orbital and spin angular momenta, respectively, $J = L + S$ is the total angular momentum and M_J is its projection along the z-axis. Since the spin-orbit energy $E_{s-o} = \beta_{LS}(\mathbf{L} \cdot \mathbf{S})$ does not depend on M_J , there are $(2S+1)(2L+1)$ degenerate states formed by linear combinations of $|JLSM_J\rangle$.

C. The Zeeman Effect [2]

The Zeeman effect in Mercury lifts the degeneracies described above and produces splittings in the spectral lines. To see this, let's consider the atomic magnetic moment, which is given by the addition of the angular and spin magnetic moments of the electron, that allows the atom to interact with an external magnetic field

$$\boldsymbol{\mu} = -\mu_B \mathbf{L} - g_s \mu_B \mathbf{S}, \quad (4)$$

where $g_s \approx 2$ is the g-factor [3]. Since the atom has a magnetic moment μ , it experiences a Lorentz force in the presence of a magnetic field \mathbf{B} , which causes it to orient itself parallel to the field. This orientation is associated with an energy [4]

$$H_{ZE} = -\mu \cdot \mathbf{B}. \quad (5)$$

As long as $E_{ZE} \ll E_{s-o} \ll E_{re}$, $|LSJM_J\rangle$ is still a valid basis and H_{ZE} can be treated as a perturbation on the ${}^{2S+1}L_J$ term levels. To find the energy of the Zeeman splitting we take expectation values of (5). Recall that $\mathbf{J}^2 |JM_J\rangle = (\mathbf{J} \cdot \mathbf{J}) |JM_J\rangle = J(J+1) |JM_J\rangle$ is the magnitude of \mathbf{J} . Therefore, we can insert $\frac{\mathbf{J} \cdot \mathbf{J}}{J(J+1)}$ into the expectation value since, in the vector model, $\langle JM_J | \frac{\mathbf{J}^2}{J(J+1)} | JM_J \rangle = 1$, to obtain

$$\begin{aligned} E_{ZE} &= -\langle LSJM_J | \mu \cdot \mathbf{B} | LSJM_J \rangle = \\ &= -\langle LSJM_J | \mu \cdot \left(\frac{\mathbf{J} \cdot \mathbf{J}}{J(J+1)} \right) \cdot \mathbf{B} | LSJM_J \rangle = \\ &= -\frac{\langle \mu \cdot \mathbf{J} \rangle}{J(J+1)} \langle \mathbf{J} \cdot \mathbf{B} \rangle = \frac{\langle \mathbf{L} \cdot \mathbf{J} \rangle + g_s \langle \mathbf{S} \cdot \mathbf{J} \rangle}{J(J+1)} \mu_B B M_J = \\ &= \underbrace{\left(\frac{3}{2} + \frac{S(S+1) - L(L+1)}{2J(J+1)} \right)}_{g_J} \mu_B B = g_J \mu_B B M_J, \quad (6) \end{aligned}$$

where $\langle \dots \rangle$ denotes expectation values in the $|LSJM_J\rangle$ basis. Now, we see that the Zeeman effect does indeed split degenerate terms because it depends on the projection of the total angular momentum M_J .

Equation (6) allows us to experimentally confirm the value of μ_B by observing the spectral splittings of Mercury in an external magnetic field. In the introduction, we mentioned that the normal Zeeman effect was explained without quantum mechanics. Here, we see that it corresponds to singlet terms $S = 0$, so the projection M_J of $\mathbf{J} = \mathbf{L}$ does not depend on the spin of the electrons. Triplet states, on the other hand, are no longer degenerate due to the Zeeman effect. The transitions corresponding to $\Delta M_J = \pm 1$ are shifted $\frac{3\mu_B B}{2}$ compared to the $\Delta M_J = 0$ transitions for the ${}^3S_1(6s7s) \rightarrow {}^3P_2(6s6p)$ transition in Mercury. The $\Delta M_J = 0$ transition are called π -transitions and emit light polarized parallel to the magnetic field, while the $\Delta M_J = \pm 1$ are called σ_{\pm} -transitions and emit circularly polarized light perpendicular to the magnetic field. The energy changes corresponding to the 3S_1 and 3P_2 term levels, respectively, are

$$\Delta E_S = 2\mu_B B \quad (7)$$

$$\Delta E_P = \frac{3}{2}\mu_B B. \quad (8)$$

Figure 2 shows all the transitions predicted by equation (6) in Mercury.

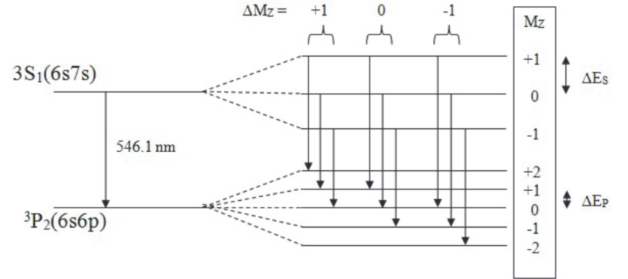


FIG. 2. 546.1nm Spectral Lines in Mercury [1]

We know that photons emitted by the atomic transitions have frequencies corresponding to the difference in energy of the initial and final states, $hf = E_S - E_P$, where h is Planck's constant and f is the frequency of light emitted. We can relate the change in energy to the wavelength λ of the emitted photon by $f = c/\lambda$. For the $M_J = 1 \rightarrow M_J = 1$ transition

$$hf_+ = (E_S + \Delta E_S) - (E_P + \Delta E_P), \quad (9)$$

and for the $M_J = -1 \rightarrow M_J = -1$ transition

$$hf_- = (E_S - \Delta E_S) - (E_P - \Delta E_P). \quad (10)$$

The difference of frequencies produced by these two transitions is given by

$$h(f_+ - f_-) = 2(\Delta E_S - \Delta E_P) = \mu_B B. \quad (11)$$

Now, we can relate (11) to the wavelengths of the emitted photons with the relations $f = c/\lambda$, where c is the speed of light,

$$hc \left(\frac{1}{f_+} - \frac{1}{f_-} \right) = \frac{hc(\lambda_- - \lambda_+)}{\lambda_- \lambda_+} = \frac{hc\Delta\lambda}{\lambda^2} = \mu_B B \quad (12)$$

$$\Delta\lambda = \frac{\mu_B B \lambda^2}{hc} \quad (13)$$

where $\lambda_- \lambda_+ = \lambda^2$ to very good approximation since the energy splittings are very small.

D. Fabry-Pérot Interferometer [1]

In the previous section, we derived the energy splittings due to the anomalous Zeeman effect and converted them to wavelengths for the ${}^3S_1(6s7s) \rightarrow {}^3P_2(6s6p)$ transitions in Mercury. Here we describe the Fabry-Pérot interferometer, which is used to produce the interference pattern, called the bull's eye pattern, that will show the spectral line splittings.

The Fabry-Pérot interferometer consists of two flat partially-reflective plates that face parallel to one another with a spacing, d , of 1.995mm. The optical cavity created in the space between the two plates, called the étalon, only allows rays that are in resonance with it to pass through by bouncing the light between the plates. The collimating lens allows rays from the source along the optical axis to pass through, but those which come in at a small angle θ from the optical axis are partially reflected. Rays that don't pass through are reflected between the two plates and interfere. The bull's eye is a result of constructive interference of light between the two plates of the interferometer.

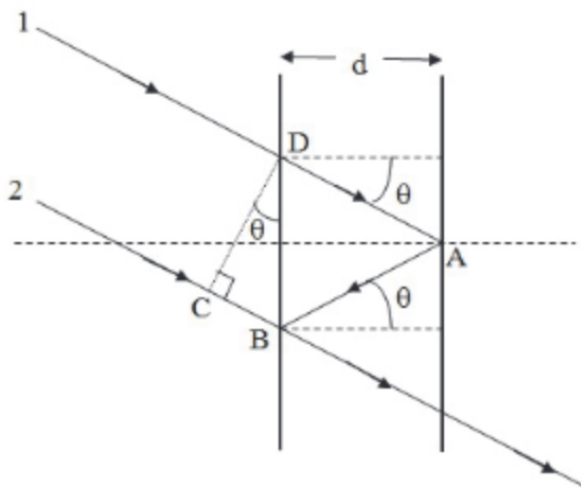


FIG. 3. Fabry-Pérot Interferometer

Figure 3 shows how light that enters the interferometer at a small angle θ off from the optical axis is reflected between the two plates to constructively interfere with rays originating from the source at the same angle. Rays one and two enter parallel to each other in the interferometer, but ray one travels farther. The difference of the distances traveled by rays one and two is

$$\begin{aligned}\Delta L &= L_{DA} + L_{AB} - L_{CB} = \\ \frac{d}{\cos \theta} + \frac{d}{\cos \theta} - 2d \sin \theta \tan \theta &= \\ \frac{2d}{\cos \theta} - \frac{2d \sin^2 \theta}{\cos \theta} &= 2d \cos \theta = \\ 2d \left(1 - \frac{\theta^2}{2}\right),\end{aligned}$$

where we have replaced $\cos \theta$ with the first two terms of its Taylor expansions since $\theta \ll 1$. The rays will constructively interfere if

$$\Delta L = (n \pm k)\lambda, \text{ where } k = 0, 1, 2, \dots \quad (14)$$

where n is a large integer, which we will see is related to the resolution of the interferometer. Equation (14) yields

$$2d \left(1 - \frac{\theta_k^2}{2}\right) = (n - k)\lambda, \text{ where } k = 0, 1, 2, \dots \quad (15)$$

The negative sign in $(n - k)$ has been taken because the left-hand side decreases as θ_k increases. The Fabry-Pérot can resolve fine detail because while changes in λ may be very small, it is multiplied by a large n , which is approximately $2d/\lambda \approx 10^4$.

E. Camera [1]

Since the angle of incidence $\theta_k = r_k/f$, where f is the focal length of the camera, is very small, the interference pattern given by equation (15) becomes

$$2d \left(1 - \frac{r_k^2}{2f^2}\right) = (n - k)\lambda, \text{ where } k = 0, 1, 2, \dots \quad (16)$$

The focal length f is unknown, but it can be found by considering the $k = 0$ ring

$$2d \left(1 - \frac{r_0^2}{2f^2}\right) = n\lambda \quad (17)$$

Subtracting equations (16) and (17), we obtain

$$C_0 = \frac{d}{f^2\lambda} = \frac{k}{r_k^2 - r_0^2}, \quad (18)$$

which is evaluated by measuring r_k and r_0 values at $B = 0$. When the magnetic field is turned on the spectral lines split into triplets. As suggested in §II, the Bohr magneton can be determined by the difference in the shifted triplet states at radii R_{k+} and R_{k-} . Plugging these radii into equation (16) and subtracting yields

$$\frac{d}{f^2}(R_{k+}^2 - R_{k-}^2) = (n - k)(\lambda_+ - \lambda_-), \quad \text{where } k = 0, 1, 2, \dots \quad (19)$$

Since n is a large integer, $(n - k)\lambda = n\lambda = 2d$ to a very good approximation. Using this fact and equation (12), we recast equation (19) as

$$\frac{d}{f^2}(R_{k+}^2 - R_{k-}^2) = \frac{2d\mu_B B \lambda}{hc}, \quad (20)$$

which is solved for the Bohr magneton to obtain

$$\mu_B = \left(\frac{C_0 hc}{2dB}\right)(R_{k+}^2 - R_{k-}^2). \quad (21)$$

Therefore, by measuring the radii R_{k+} and R_{k-} , which change as a function of the magnetic field B , we can determine the Bohr magneton.

III. EXPERIMENTAL METHODS

A. Materials

The experimental setup, depicted below, consists of a DC power supply that powers an electromagnet, which houses a pen-type Mercury lamp in its center, a polarizer, Fabry-Pérot interferometer and a camera fixed on a track for fastening each element in place.

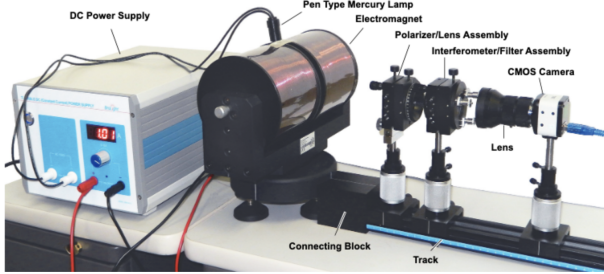


FIG. 4. Experimental Setup [1]

The electromagnet has a maximum input current of 6A, which corresponds to a magnetic field of about 1.200T according to the test report (see Appendix C). It consists of two parallel cylindrical coils, which create a constant magnetic field passing through the Mercury lamp sitting in between them.

The pen-type Mercury lamp is a gas-discharge lamp that contains Mercury gas within a glass tube. The lamp conducts current flowing from the DC power source, which heats up the Mercury and creates an electric arc once the Mercury is vaporized. The lamp conducts currents up to 145mA and has an output of 1500V.

A quarter-wave plate is placed on the track in front of the electromagnet for certain measurements. It can convert linearly polarized light, which enters at 45° , to circularly polarized light. With this device we can observe the π - and σ_\pm -transitions at the same time. This filtering is depicted in figure 5.

In front of the quarter-wave plate is a linear polarizer that can filter out circularly polarized light, which is used to observe the π -transitions that emit only linearly polarized light. When the linear polarizer is at 0° no light is filtered and we observe the triplet splittings. When the polarizer is at 90° only linearly polarized light passes through and we observe doublets corresponding to the π -transitions.

The light from the polarizer then passes through the Fabry-Pérot interferometer, which has a spacing $d = 1.995\text{mm}$ between plates and are parallel to a high degree of accuracy, to produce the interference pattern that is measured and used to calculate the Bohr magneton. The interferometer was explained above, but, in short, it only allows light in resonance with it to pass through while bouncing the rest of the light between its mirrors, again only allowing constructively interfering light to pass through, to produce an interference pattern. The

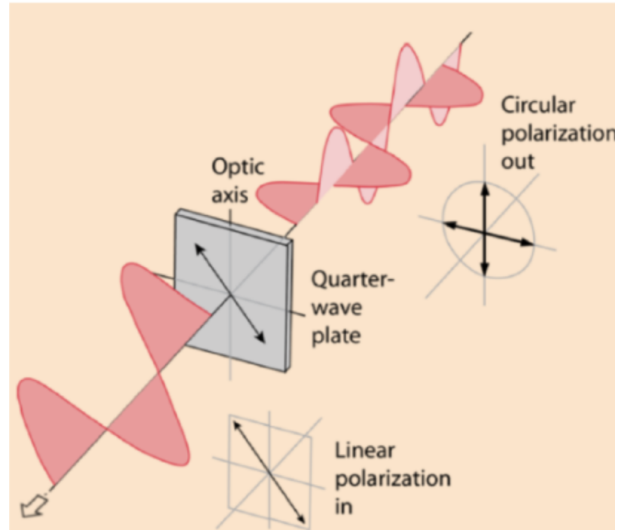


FIG. 5. Quarter-Wave Plate [1]

interference pattern is a series of concentric rings corresponding to phase shifts of $k2\pi$, where k is the ring index.

Finally, we use a camera to capture the image produced by the interferometer, which is connected to the PASCO data collection software.

B. Setup

The polarizer, interferometer and camera were placed at the 30, 40 and 57cm marks, respectively, on the track. While the focal length of the camera was not known a priori, its position was varied to obtain the best picture possible. The polarizer is initialized at 0° , which allows us to see triplets. The electromagnet was initially positioned so that light emitted perpendicular to the magnetic field was observed. In this configuration, the magnetic field was varied by increasing the current supplied between 0A and 6A at intervals of 1A for the first run, and again with the polarizer at 90° , which filters out circularly polarized light and produces the doublet patterns, for the second run.

For the third and final run, the electromagnet was rotated so that the light emitted parallel to the magnetic field was observed. The quarter-wave plate was also placed on the track directly in front of the electromagnet, which reduced the light intensity by a factor of two, and the magnetic field was varied in the same way.

In summary, light originated from the pen-type Mercury lamp emissions in the center of the electromagnet at the end of the track. The light emitted perpendicular to the magnetic field was observed during rounds one and two, and parallel to the magnetic field during round three. If a quarter-wave plate was placed on the track (run three), circularly polarized light became linearly polarized and vice versa. Then the light passed

through the linear polarizer, which filtered out circularly polarized light during the second run. In every run, light then passed through the Fabry-Pérot interferometer, which created the bull's eye pattern by using partially-reflective parallel plates to constructively interfere light. The light then terminates in the lens of the camera, which was connected to the PASCO computer application to capture photos of the interference pattern for analysis. This summary of the path that light takes throughout the experiment provides a full summary of the experimental configuration.

The pictures obtained were analyzed using the PASCO software. The radius tool was used to measure the radii of the rings produced by spectral line splittings. Then PASCO's data analysis features were used to input the data and quickly compute the Bohr magneton.

IV. RESULTS AND DISCUSSION

Using PASCO's image analysis software, we measured the radii of triplet lines in the green spectrum of Mercury produced by $^3S_1(6s7s) \rightarrow ^3P_2(6s6p)$ transitions. Spectral line splittings were observed when the magnetic field was about 0.941T, which corresponds to a current of 3A. Figure 6 shows the radii of the triplet levels as a function of the current supplied to the electromagnet for rings $k = 0, 1, 2, 3$ when the polarizer was oriented at 0° and the light is emitted perpendicular to the magnetic field. In this configuration, we observe light that is polarized parallel to the magnetic field, namely light emitted by the π -transitions. When the polarizer is at 0° and is parallel with the magnetic field the linearly polarized light emitted by the π -transitions is allowed to pass and we observe the triplet splittings. When the polarizer is turned through 90° , however, the linearly polarized light is not allowed to pass through and we don't see the triplets produced by π -transitions. The σ_{\pm} transitions are also responsible for the observation of triplets in this configuration. When seen edge-on the circular motion is collapsed to one longitudinal component, which emits linearly polarized light that can pass through the polarizer and be used by the Fabry-Pérot interferometer to produce an interference pattern [2]. Since only one component of the circular motion is observed at this orientation, however, the intensity is reduced and the inner and outer rings associated with the triplet splittings appear fainter than the central rings produced by the π -transitions.

When the electromagnet was positioned parallel to the light emitted by the Mercury lamp the intensity was reduced by a factor of two by the quarter-wave plate. The light emitted by the π -transitions cannot be observed from the direction because we are viewing the linear motion of electrons responsible for those transitions head-on so that their motion cannot be seen. From this orientation, we can see the full rotational motion of electrons that undergo σ_{\pm} -transitions, which makes the intensity of their light greater than before when the light was per-

pendicular to the magnetic field. The σ_{\pm} -transitions emit circularly polarized light, which is converted to linearly polarized light by the quarter-wave plate that can be used by the Fabry-Pérot interferometer to produce the observed interference pattern.

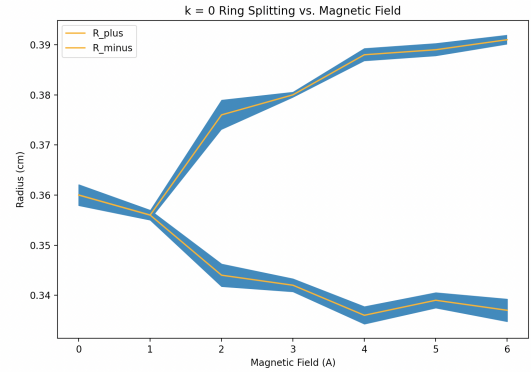


FIG. 6. $k = 0$ ring splitting as a function of the perpendicular magnetic field B with polarizer at 0°

Figure 6 shows the triplet splitting in the central $k = 0$ that begins at 2A. The top band is the radius of the upper triplet level corresponding to the σ_+ -transition and the bottom corresponds to the σ_- -transition. The blue fringe shows one standard deviation above and below the R_+ and R_- lines, which was computed using four independent measurements of each radius. The data used to produce figure 6 can be found in the appendix. Figure 6 also shows that the center of the rings does not move even as the magnetic field is varied. This justifies the simplifying assumption made in §II. Theory that $E_{ZE} \ll E_{s-o} \ll E_{re}$ in order to treat the Zeeman Hamiltonian as a perturbation on the $|LSJM_J\rangle$ states. This assumption is confirmed by the experiment since the positions of the rings don't change and the triplets occur in roughly the same positions as the original rings. Since the triplet splittings are much smaller than the overall scale of the system, they can safely be treated in the way discussed in §II.

The measurements of the radial positions of the rings as shown in figure 6 and listed in the table in the appendix are used with equation 21 to calculate the Bohr magneton. Using four independent measurements of the radial positions of R_+ and R_- for the ring $k = 0$ for magnetic fields corresponding to currents of 3, 4, 5, 6A. The average Bohr magnet for these trials is $5.17 \pm 0.69 \times 10^{-24} \text{ J/T}$. The calculated Bohr magneton is correct to the order of magnitude of the real value, however, it is off by 79%, which is quite significant. The standard deviation of $0.69 \times 10^{-24} \text{ J/T}$ cannot explain this discrepancy, so there must have been systematic errors. The most glaring error is related to the optical alignment, which is immediately obvious from the interference patterns provided in Appendix B. The optical alignment is very hard to get just right and is also hard to maintain since not

each part of the experimental setup, such as the camera, can be fixed so any movement may disturb the alignment. Misalignment causes distortion so that a large part of the rings is blurred and skewed, which causes the measured radii to be larger than they are in reality. The well-resolved parts of the ring, mainly the top, are realistic due to the accuracy of the Fabry-Pérot interferometer. The Fabry-Pérot interferometer is another source of error since it changes the path of the light emitted by the Mercury lamp, however, its high degree of accuracy previously discussed means that any errors are very small. Additionally, the Fabry-Pérot interferometer would be the only source of propagating errors, but its high degree make any errors negligible. We can see from equation 21 that the main source of error comes from radius measurements

$$\Delta\mu_B = \left(\frac{C_0 hc}{2dB} \right) (2R_{k,+}\Delta R_{k,+} + 2R_{k,-}\Delta R_{k,-}), \quad (22)$$

which is underestimated by the standard deviation. Additionally, we found the test report (see Appendix C) for the electromagnet to be slightly inaccurate upon verification of the magnetic field strength in between the two coils with a Hall meter. The magnetic field corresponding to a current of 3A was measured with the Hall meter to be about 0.875T as opposed to 0.941T according to the test report. The experiment can be improved by having a fixed optical setup that is better aligned.

V. CONCLUSION

In conclusion, the value of the Bohr magneton was found by using the Zeeman effect, which causes splittings in the green spectrum of Mercury. These splitting are produced by atomic transitions of electrons in Mercury's valence shell, which have magnetic moments due to their spin and orbital angular momentum. By using optical physics to obtain interference patterns with light emitted by electrons undergoing transitions we were able to indirectly measure magnetic properties of the electron and, thus, the value of the Bohr magneton. The measured value of the Bohr magneton, while on scale, differs dramatically from the true version. This is due to the difficulty of obtaining a perfect optical alignment. While a perfect interference pattern may be hard to maintain, certain adjustments to the experimental setup, such as components that are better fastened, would result in more accurate measurements and results.

Appendix A: Data Tables

Current (A)	Ring Radius Measurements (m)								R_{3+}
	R_{0-}	R_{0+}	R_{1-}	R_{1+}	R_{2-}	R_{2+}	R_{3-}		
0.0	0.36	0.36	0.36	0.36	0.363	0.363	0.358	0.358	0.358
1.0	0.356	0.356	0.357	0.357	0.356	0.356	0.358	0.358	0.358
2.0	0.344	0.376	0.342	0.378	0.34	0.383	0.339	0.378	0.378
3.0	0.342	0.38	0.339	0.381	0.34	0.38	0.34	0.381	0.381
4.0	0.336	0.388	0.339	0.386	0.34	0.387	0.338	0.389	0.389
5.0	0.339	0.389	0.34	0.39	0.337	0.387	0.337	0.388	0.388
6.0	0.337	0.391	0.335	0.392	0.338	0.39	0.333	0.392	0.392

TABLE I. Measurements of the radius of circles with Perpendicular Magnetic Field and Polarizer at 0°

Appendix B: Equipment Documentation

Current (A)	Magnetic Field Strength (T)
0.5	0.219
1.0	0.435
1.5	0.641
2.0	0.777
2.5	0.869
3.0	0.941
3.5	1.001
4.0	1.052
4.5	1.098
5.0	1.138
5.5	1.175

TABLE II. Electromagnet Test Report

Appendix C: Interference Patterns

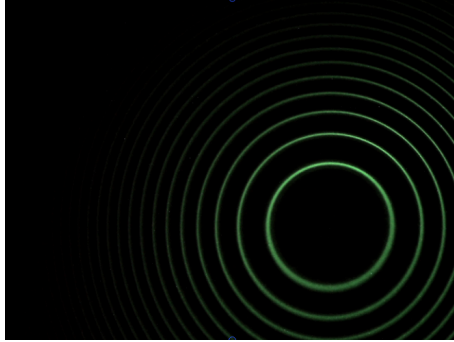


FIG. 7. Perpendicular Magnetic Field, $I = 0\text{A}$, Polarizer at 0°

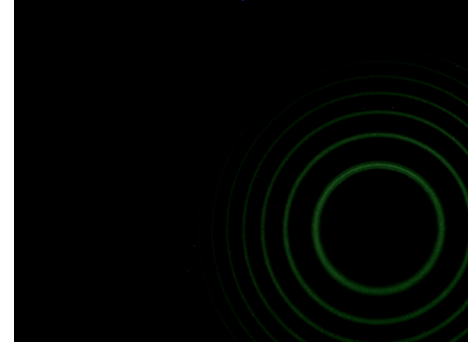


FIG. 10. Perpendicular Magnetic Field, $I = 3\text{A}$, Polarizer at 0°

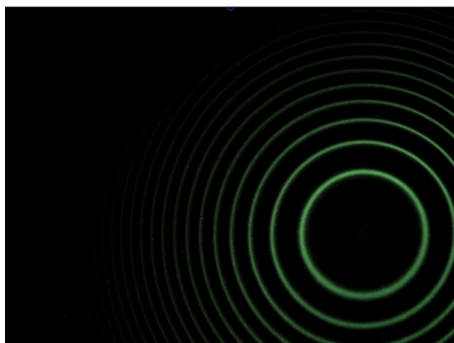


FIG. 8. Perpendicular Magnetic Field, $I = 1\text{A}$, Polarizer at 0°

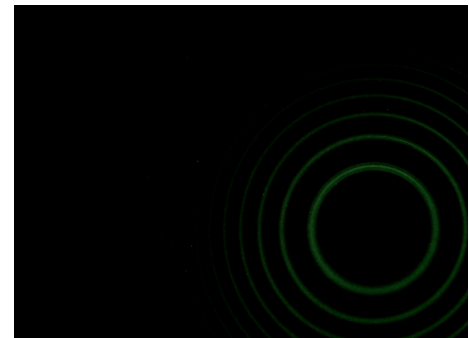


FIG. 11. Perpendicular Magnetic Field, $I = 4\text{A}$, Polarizer at 0°

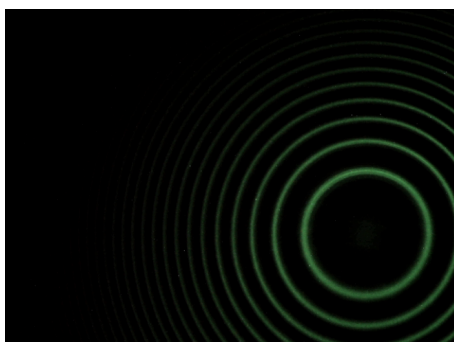


FIG. 9. Perpendicular Magnetic Field, $I = 2\text{A}$, Polarizer at 0°

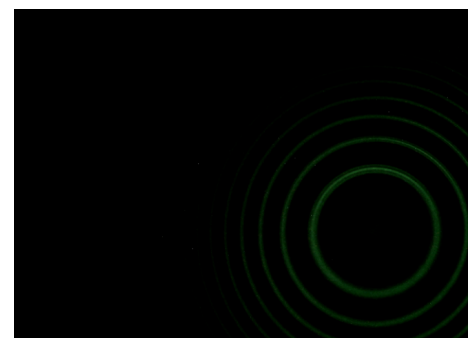


FIG. 12. Perpendicular Magnetic Field, $I = 5\text{A}$, Polarizer at 0°

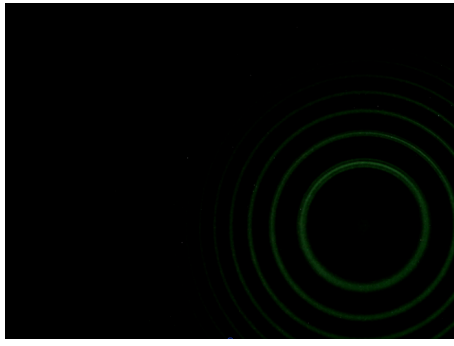


FIG. 13. Perpendicular Magnetic Field, $I = 6\text{A}$, Polarizer at 0°

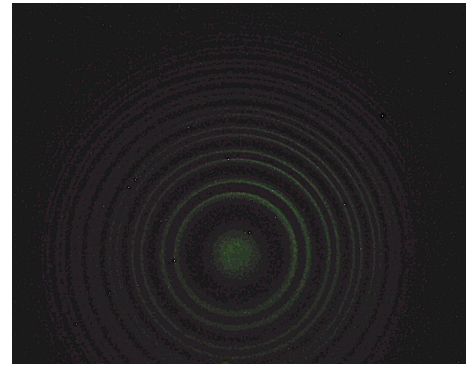


FIG. 17. Parallel Magnetic Field, $I = 3\text{A}$, Polarizer at 0°

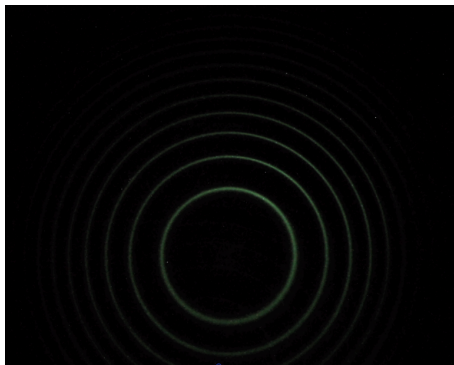


FIG. 14. Parallel Magnetic Field, $I = 0\text{A}$, Polarizer at 0°

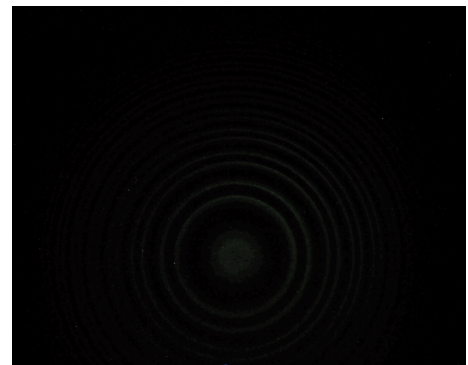


FIG. 18. Parallel Magnetic Field, $I = 4\text{A}$, Polarizer at 0°

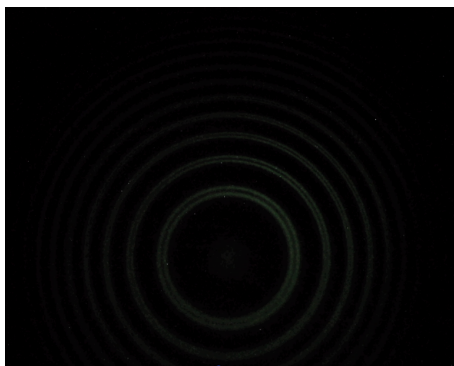


FIG. 15. Parallel Magnetic Field, $I = 1\text{A}$, Polarizer at 0°

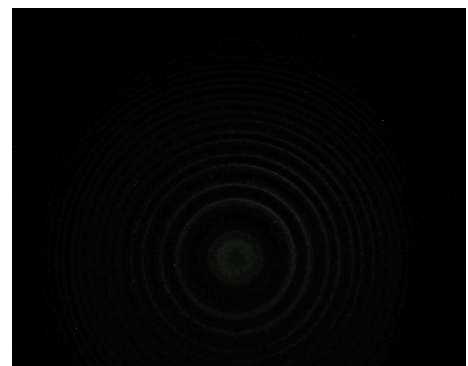


FIG. 19. Parallel Magnetic Field, $I = 5\text{A}$, Polarizer at 0°



FIG. 16. Parallel Magnetic Field, $I = 2\text{A}$, Polarizer at 0°

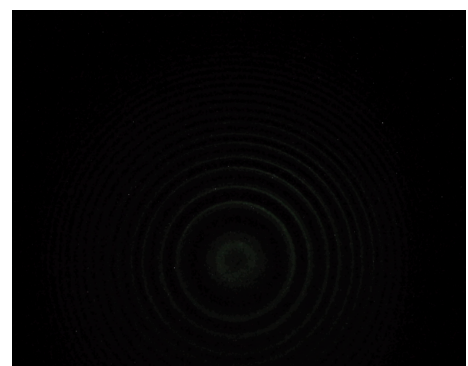


FIG. 20. Parallel Magnetic Field, $I = 6\text{A}$, Polarizer at 0°

-
- [1] P. Broglie Technology Co., Ltd, “Zeeman effect experiment: Model se-9654,” 2022. https://cdn.pasco.com/product_document/Zeeman-Effect-Experiment-Manual-SE-9654.pdf, Accessed 16 September 2023.
 - [2] C. Foot, *Atomic Physics*. Oxford University Press, 2005.
 - [3] S. Blundell, *Magnetism in Condensed Matter*. Oxford University Press, 2001.
 - [4] J. Townsend, *A Modern Approach to Quantum Mechanics, Second Edition*. University Science Books, 2012.